Elevation-Dependent Trends in Precipitation Observed during NAME

ANGELA K. ROWE, STEVEN A. RUTLEDGE, TIMOTHY J. LANG, PAUL E. CIESIELSKI, AND STEPHEN M. SALEEBY

Department of Atmospheric Science, Colorado State University, Fort Collins, Colorado

(Manuscript received 28 September 2007, in final form 7 April 2008)

ABSTRACT

Radar data from the 2004 North American Monsoon Experiment (NAME) enhanced observing period were used to investigate diurnal trends and vertical structure of precipitating features relative to local terrain. Two-dimensional composites of reflectivity and rain rate, created from the two Servicio Meteorológico Nacional (SMN; Mexican Weather Service) C-band Doppler radars and NCAR's S-band polarimetric Doppler radar (S-Pol), were divided into four elevation groups: over water, 0–1000 m (MSL), 1000–2000 m, and greater than 2000 m. Analysis of precipitation frequency and average rainfall intensity using these composites reveals a strong diurnal trend in precipitation similar to that observed by the NAME Event Rain Gauge Network. Precipitation occurs most frequently during the afternoon over the Sierra Madre Occidental (SMO), with the peak frequency moving over the lower elevations by evening. Also, the precipitation events over the lower elevations are less frequent but of greater intensity (rain rate) than those over the SMO. Precipitation echoes were partitioned into convective and stratiform components to allow for examination of vertical characteristics of convection using data from S-Pol. Analyses of reflectivity profiles and echo-top heights confirm that convection over the lower terrain is more intense and vertically developed than convection over the SMO. Warm-cloud depths, estimated from the Colorado State University–NAME upper-air and surface gridded analyses are, on average, 2 times as deep over the lower terrain as compared with over the SMO. Using a simplified stochastic model for drop growth, it is shown that these differences in warm-cloud depths could possibly explain the observed elevation-dependent trends in precipitation intensity.

1. Introduction

The onset of the North American monsoon (NAM) during mid- to late June marks a shift in warm-season climate, characterized primarily by an abrupt transition from relatively hot, dry weather to cooler, rainy conditions in the semiarid regions of southwestern United States and western Mexico (e.g., Douglas et al. 1993; Adams and Comrie 1997). The arrival of strong convection in this region has also been linked to a decrease in precipitation over the Great Plains in the United States (e.g., Douglas et al. 1993; Mock 1996; Higgins et al. 1997) and to an increase in rainfall over the East Coast of the United States (e.g., Higgins et al. 1997). Accurate modeling and prediction of the establishment and variability of the NAM is crucial not only for improved warm-season forecasting but also for management of water resources, which is especially important for regions in northwestern Mexico, where 50%–80% of the annual water resource is received from monsoon precipitation (Gochis et al. 2006).

The main goal of the North American Monsoon Experiment (NAME) is to better understand and model precipitation processes occurring in the core region of the NAM for improved prediction of warm-season rainfall (Higgins et al. 2006). The local topography of this core area in northwestern Mexico is dominated by the Sierra Madre Occidental (SMO), which extends to over 3000 m (MSL; Fig. 1) and has been found to have important impacts on the diurnal cycle of monsoon precipitation in this region (e.g., Gochis et al. 2003, 2004; Lang et al. 2007). The diurnal trend of rainfall is generally characterized by the initiation of convection over the peaks and western foothills of the SMO during the late afternoon (Lang et al. 2007), followed by a westward propagation and upscale growth into mesoscale convective systems (MCSs) during the late evening/

Corresponding author address: Angela K. Rowe, Department of Atmospheric Science, Colorado State University, Fort Collins, CO 80523.
E-mail: arowe@atmos.colostate.edu

DOI: 10.1175/2008MWR2397.1

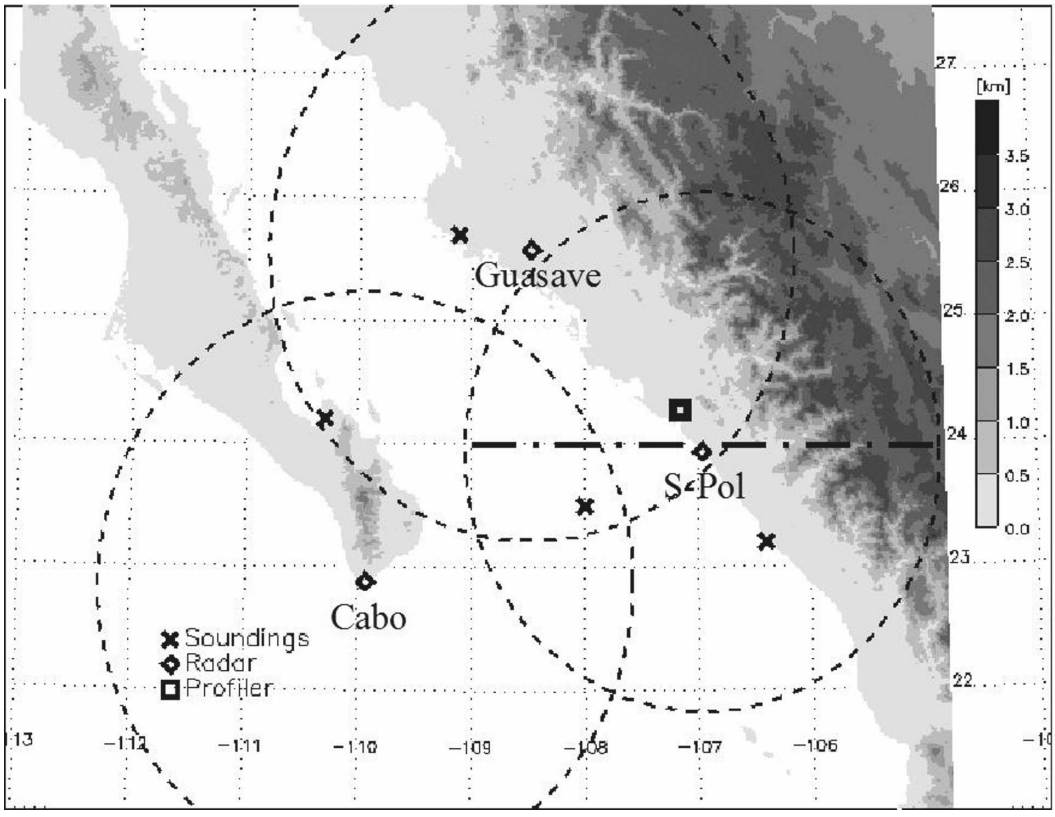

FIG. 1. NAME radar network domain with 2D gridded topography shaded by 500-m increments. Diamonds denote the location of the three radars, and dashed circles represent the range of each radar. Sounding locations are represented by Xs, including Mazatlan (23.2°N, 106.4°W), Los Mochis (25.7°N, 109.1°W), and La Paz (24.2°N, 110.3°W). The square shows the location of the wind profiler, and the dash–dotted line indicates the cross section for Fig. 13.

early morning hours (Farfán and Zehnder 1994; Janowiak et al. 2005; Lang et al. 2007). For example, Lang et al. (2007) found that precipitation occurring over the Gulf of California is approximately 12 h out of phase with precipitation over the SMO. This diurnal cycle is phase shifted a few hours in global and regional models compared to the observations (Collier and Zhang 2007); therefore, crucial questions need to be addressed regarding the preferred location of convective initiation along the SMO, frequency and intensity of rainfall, and the evolution of the precipitating features in relation to local forcing in order to improve simulations of the diurnal cycle in numerical models (Lang et al. 2007).

The 2004 NAME field campaign included a variety of observational platforms and instrumentation, such as surface stations, a research vessel, satellites, wind profilers, an upper sonde network, rain gauge networks, radars, and a research aircraft, among others (Higgins et al. 2006). These platforms provided a wealth of data to analyze both the horizontal and vertical characteristics of precipitation. Data from the NAME Event Rain Gauge Network (NERN)—consisting of 87 automatic-recording, tipping-bucket rain gauges positioned along six transects—highlighted a strong dependence of precipitation frequency and intensity on elevation (Gochis et al. 2004). These results revealed two main daily and subdaily precipitation features: 1) a core region of frequent but moderate-intensity precipitation over the high terrain of the SMO, and 2) an elevation-dependent diurnal cycle of precipitation where rainfall occurs earliest and most frequently over the higher elevations and later in the afternoon/evening and overnight across lower elevations, but with less frequency and higher intensity (Gochis et al. 2004). Gochis et al. (2007) stated that the NERN dataset likely captures the essential features of rainfall; however, because of the sparse coverage of the NERN data, it is useful to explore precipitation characteristics using radar data, which are more continuous in space. For this reason, as well as the obvious lack of vertical information from the NERN data, radar data are needed to further examine the structure, kinematics, and morphology of convection, including

the diurnal cycle of precipitating clouds within the core monsoon region (Lang et al. 2007). This study uses data provided by the NAME radar network to investigate the elevation-dependent trends in NAM precipitation in greater detail than rain gauge information allows, with an emphasis on vertical characteristics of convection in this region.

2. Data and methodology

a. NAME radar network

The NAME enhanced observing period (EOP) occurred July through August 2004, during which three ground-based radars were operational in northwestern Mexico (Higgins et al. 2006; Lang et al. 2007). The network consisted of the National Center for Atmospheric Research's (NCAR) S-band polarimetric Doppler radar (S-Pol), located along the Gulf of California coast, and two C-band Doppler radars (digitized for NAME) operated by the Servicio Meteorológico Nacional (SMN; Mexican Weather Service): Guasave, located north of S-Pol along the coast, and Cabo, located at the tip of the Baja peninsula (Fig. 1). S-Pol operated at two main pulse repetition frequencies: 720 Hz (most common) and 960 Hz, providing maximum unambiguous ranges of approximately 210 and 150 km, respectively. Data from S-Pol were acquired from 8 July to 21 August 2004. S-Pol scans included a set of low-angle 360° surveillance scans, with elevation angles of 0.8°, 1.3°, and 1.8°, for rain mapping to the maximum range of roughly 210 km, and a set of full volume scans extending to higher elevation angles to describe the vertical structure of precipitation. Also, sector volume scans, with azimuthal widths between 90° and 120°, were obtained for 36 cases (comprising about 95 h of scan time) to document the detailed temporal evolution of individual precipitating features. The SMN radars scanned at a single, fixed elevation angle, the choice of angle varying between 0.5°, 1.0°, and 1.5° for Guasave and fixed at 0.6° for Cabo. These radars provided coverage to a maximum unambiguous range of nominally 230 km. Data from the Cabo and Guasave radars were processed for the same time frame as the S-Pol operations, although data from Guasave were not available for most of the period during 22–31 July because of recording problems (Lang et al. 2007).

b. Two-dimensional composites

A considerable amount of quality control was applied to data from all three radars, as detailed in Lang et al. (2007). Further details regarding the radar data can be found at http://data.eol.ucar.edu/datafile/nph-get/82.119/readme_NAME_regional_radar_composites_v2.1.pdf. The radar data were interpolated from the original polar-coordinate format to a two-dimensional spherical grid. Sweep files from the lowest elevation angles at approximately the same time were combined to create composites available every 15 min from 8 July 0000 UTC through 21 August 2345 UTC at a 0.02° latitude–longitude resolution. The 2D composites used in this study included Geostationary Operational Environmental Satellite (GOES) infrared brightness temperature (to filter sea clutter near the Cabo radar), near-surface reflectivity, and near-surface rain rate. For grid points where radar gates overlapped, the lowest elevation gate took precedence (Lang et al. 2007). S-Pol rain rates were computed using a modified version of the Colorado State University (CSU) blended rainfall algorithm (Cifelli et al. 2002), and rain rates for Cabo and Guasave were computed using a reflectivity–rain rate (Z–R) relationship of $Z = 133R^{1.5}$ (Z, mm^6 m^{-3}; R, mm h^{-1}), derived from a polarimetrically tuned approach to the S-Pol data (Bringi et al. 2004). Rain rates were capped at 250 mm h^{-1} in order to reduce ice contamination. Information obtained from these 2D composites was valuable for analyzing diurnal trends in precipitation frequency and intensity across a relatively large portion of the NAME tier I region.

c. Three-dimensional dataset

A three-dimensional Cartesian dataset was created using only S-Pol data to allow for examination of the vertical structure of precipitating features. The horizontal range of this 3D dataset extended roughly 160 km from S-Pol in all directions, with a vertical resolution of 1 km. This information was available at a 15-min temporal resolution, and at the same 0.02° latitude/longitude horizontal resolution as the two-dimensional composites to allow for comparison with the horizontal view of precipitation. All major polarimetric variables were available from this 3D dataset, including reflectivity, differential reflectivity, specific differential phase, linear depolarization ratio, and correlation coefficient (e.g., Doviak and Zrnic 1993, chapter 6) and were used for quality control of the data. Only the reflectivity field was used for analyses in this study; however, future studies will be devoted to the use of this polarimetric information for further understanding of microphysical processes in this region.

d. Topographic data

Topographic data from the National Geophysical Data Center (NGDC) were also available on a 0.02° grid spacing, with elevation given in meters MSL. This

dataset was separated into four elevation groups (over water and over land with the following elevation increments, 0–1000 m, 1000–2000 m, and greater than 2000 m) in order to examine the characteristics of precipitation over the coastal areas and water in relation to over the SMO. This specific grouping of elevation was chosen to correspond to the low, middle, and high elevation groups used for the NERN data (Gochis et al. 2004). A shift of 500 m in the group thresholds (e.g., 0–500 m, 500–1500 m, and >1500 m) produced similar trends to those observed in this study; therefore, the results were not highly dependent on the elevation grouping of choice.

e. Convective-stratiform partitioning

A partitioning scheme, following the algorithm described by Steiner et al. (1995) with modifications by Yuter and Houze (1997, 1998), was applied to each grid point on the 2D reflectivity composites with reflectivity greater than 0 dBZ to distinguish between convective and stratiform precipitation. Grid points were first partitioned based on an absolute criterion, for which the grid point was classified as convective if it exceeded a threshold of 40 dBZ (e.g., Steiner et al. 1995; DeMott and Rutledge 1998; Rickenbach and Rutledge 1998; Cifelli et al. 2002). If the grid point reflectivity was <40 dBZ, a gradient criterion was applied for which the reflectivity at that grid point had to exceed the parameter ΔZ, defined as

$$\Delta Z = a\cos[(\Pi Z_{\mathrm{bg}})/2b],$$

where Z_{bg} was the average reflectivity within an 11-km radius of that grid point, and a and b were user-specified parameters to optimize performance for the given dataset. For this study, a and b were 8 and 150 [as compared with 8 and 64 used originally in Yuter and Houze (1997, 1998)], respectively, based on detailed tests of the classification for a variety of cases from the NAME radar dataset, including scattered convection, linear features, large mesoscale convective systems, and stratiform precipitation with embedded convection. Once both criteria were applied to each grid point, the partitioning algorithm set a convective radius around each convective grid point, based on background reflectivity (Z_{bg}), and each point within this radius was also classified as convective. For this study, the thresholds for Z_{bg} were decreased by 5 dBZ [relative to Yuter and Houze (1997, 1998)] to compensate for convection that was incorrectly classified because of altering the b parameter.

3. Elevation-dependent trends in rainfall intensity and frequency

a. Precipitation intensity as a function of terrain

The elevation-dependent trends in precipitation are first investigated using cumulative distribution functions of 15-min (greatest temporal resolution possible from the radar data) and 24-h rainfall totals (mm). The 2D rain-rate composites from the NAME radar network were used to obtain 15-min rainfall totals, which were then binned from 0 to 84 mm by 2-mm increments, and 24-h rainfall totals, binned from 0 to 270 mm by 5-mm increments. The largest 15-min rainfall totals (Fig. 2a) occur in the 0–1000- and 1000–2000-m elevation ranges, whereas the higher peaks over the SMO (>2000 m) are characterized by a greater fraction of lighter precipitation. This is consistent with results drawn from NERN data, which found that, for 10-min event rain totals, there was a clear progression toward a greater number of heavier precipitation events with decreasing elevation (Gochis et al. 2007).

Figure 2b shows a similar trend with the greatest 24-h rainfall accumulations occurring over elevations below 2000 m, with lower daily totals contributing to a greater fraction of precipitation over the SMO (>2000 m). It is evident, however, that a greater separation between elevation groups exists for daily totals compared to 15-min totals. The lesser separation for 15-min totals indicates that precipitation may be intense both over the coast and over the SMO (>2000 m), but the much greater difference in daily totals between elevation groups suggests that precipitation over the lower elevations has a longer duration than over the peaks of the SMO. A similar trend was observed by the NERN, for which Gochis et al. (2007) suggested the potential for the foothills of the SMO to receive brief periods of intense rainfall, but these intense rates are not sustained as long as over or nearer to the coast.

b. Hourly rainfall statistics

Negri et al. (1994) first identified the diurnal cycle of precipitation within the core North American monsoon region using rainfall estimates derived from Special Sensor Microwave Imager (SSM/I) observations. This cycle is characterized by convective initiation over the peaks and western slopes of the SMO during the afternoon, and the occurrence of convection offshore during the early morning hours (consistent with the radar-based study of Lang et al. 2007). Because monsoon precipitation is greatly influenced by the local topography, hourly rainfall intensities and precipitation frequency were examined using the rain rates from the

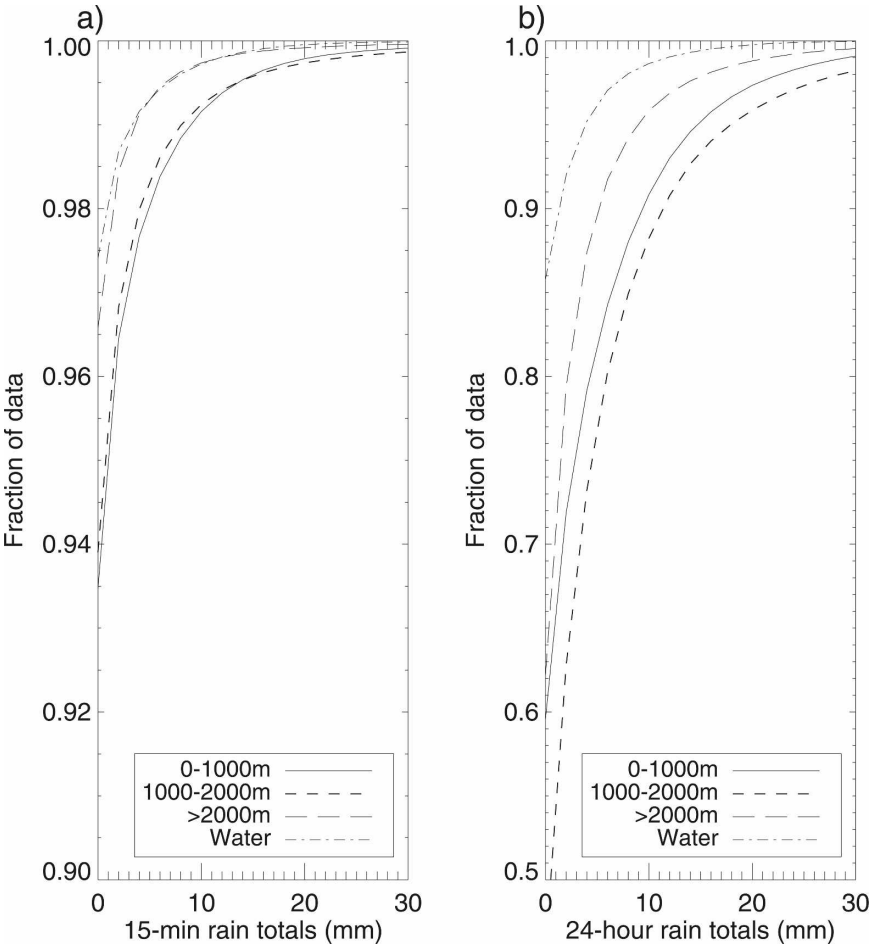

FIG. 2. Cumulative distribution functions calculated for (a) 15-min rain totals and (b) 24-h rain totals. Values are computed over the entire 2D composite domain for every available radar volume scan.

2D radar composites to further investigate elevation-dependent diurnal trends in precipitation.

Figure 3a shows the median hourly conditional rainfall rates over the NAME radar domain; median rates were used instead of means to eliminate the influence of outliers in the dataset. Figure 3b displays the precipitation frequency as a function of topography and local daylight time (LDT; UTC − 6), normalized by the total number of radar points (raining and nonraining) available in each elevation group for all 2D composites. Similar to the NERN results, these plots show the initiation of convection over the SMO during the afternoon and the tendency for greater intensity, but less frequent precipitation events to occur during the early morning hours over the low terrain (Gochis et al. 2004). More specifically, precipitation occurs most frequently at 1600 LDT over the SMO (Fig. 3b), where convection initiates over the high terrain (Fig. 3a). The highest frequencies continue to be associated with precipitation over the western slopes of the SMO as the day progresses and are characterized by the greatest median rainfall intensities until after midnight when precipitation is most intense and frequent over the coast (0–1000 m).

Diurnal characteristics of precipitation are further investigated in Fig. 4 with plots of 6-h total rainfall (in mm) beginning at 0000, 0600, 1200, and 1800 LDT, normalized by the number of observations. These plots show the largest amount of total rainfall occurring over the coastal plain at local midnight into the early morning. The initiation of afternoon convection over the SMO is reflected by greater totals in the higher elevations by noon and extending through 1700 LDT. In the evening (1800–2300 LDT), precipitation again tends to be confined to the lower elevations as the afternoon convection moves toward the coast and over water as the day progresses. This emphasizes the trend of greatest rainfall amounts occurring over the coast, particu-

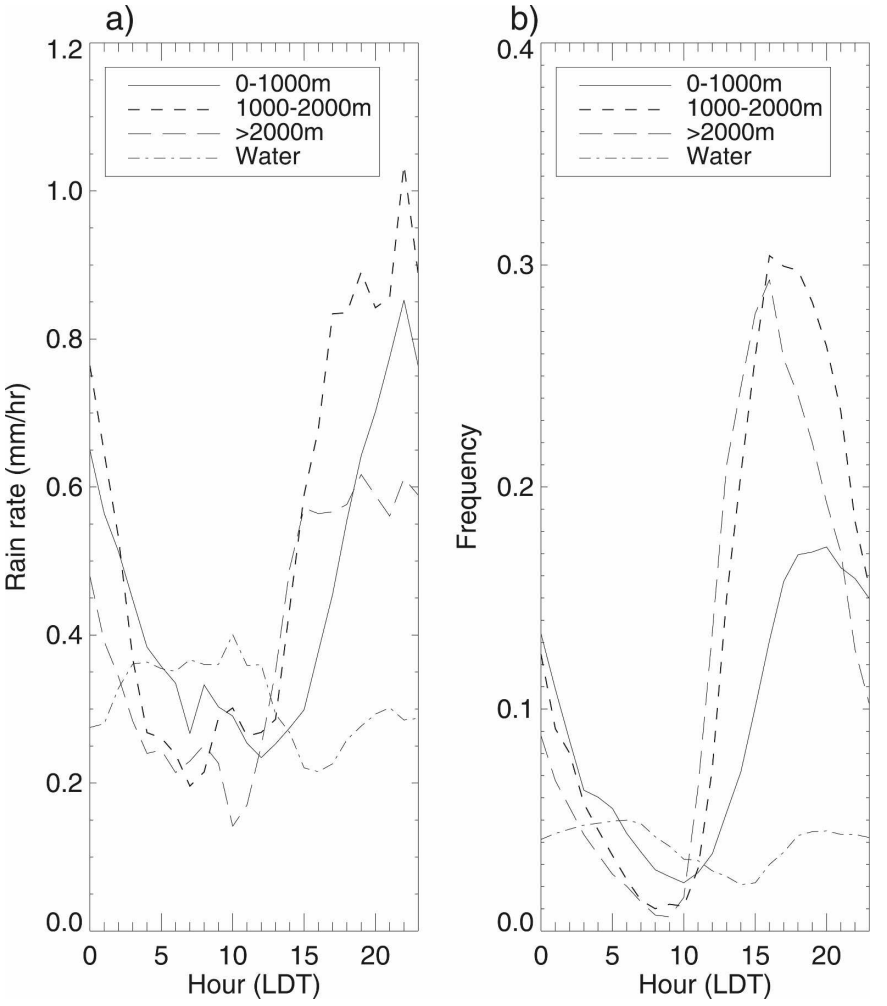

FIG. 3. Hourly plots (LDT) of (a) median rainfall intensity including only rain rates greater than 0 mm h^{-1} and (b) precipitation frequency, normalized by all available grid points covered by the radar in the specific elevation group.

larly during the overnight hours, and frequent afternoon convection over the SMO producing relatively less rainfall, especially over the highest terrain. Gochis et al. (2003) related this cycle to daily mountain–valley circulations, describing an enhancement of afternoon convection over the SMO by onshore and upslope moist flow from the Gulf of California. Once the upslope flow reverses with decreased solar insolation, a westward-propagating zone of convergence is generated, aiding in the movement of convection over the coast and Gulf of California by the early morning (Gochis et al. 2003). Also, low-level environmental shear was found to be important for the upscale growth and longer life cycles of precipitating features as they move toward the coast (Lang et al. 2007), although this is also a topic of ongoing research.

It is encouraging that this elevation-dependent diurnal cycle of precipitation intensity and frequency obtained from radar data agrees with previous findings from the comparatively sparse NERN (Gochis et al. 2004), therefore validating those results and providing greater confidence in the understanding of the diurnal precipitation trends using an independent dataset. In addition, radar data allows for the vertical characteristics of precipitation as a function of terrain to be examined.

4. Vertical characteristics of precipitation

a. Mean reflectivity profiles

The 3D dataset created from S-Pol is used to analyze the vertical characteristics of convection during NAME to examine possible elevation-dependent trends. Each grid point was subjected to the previously described

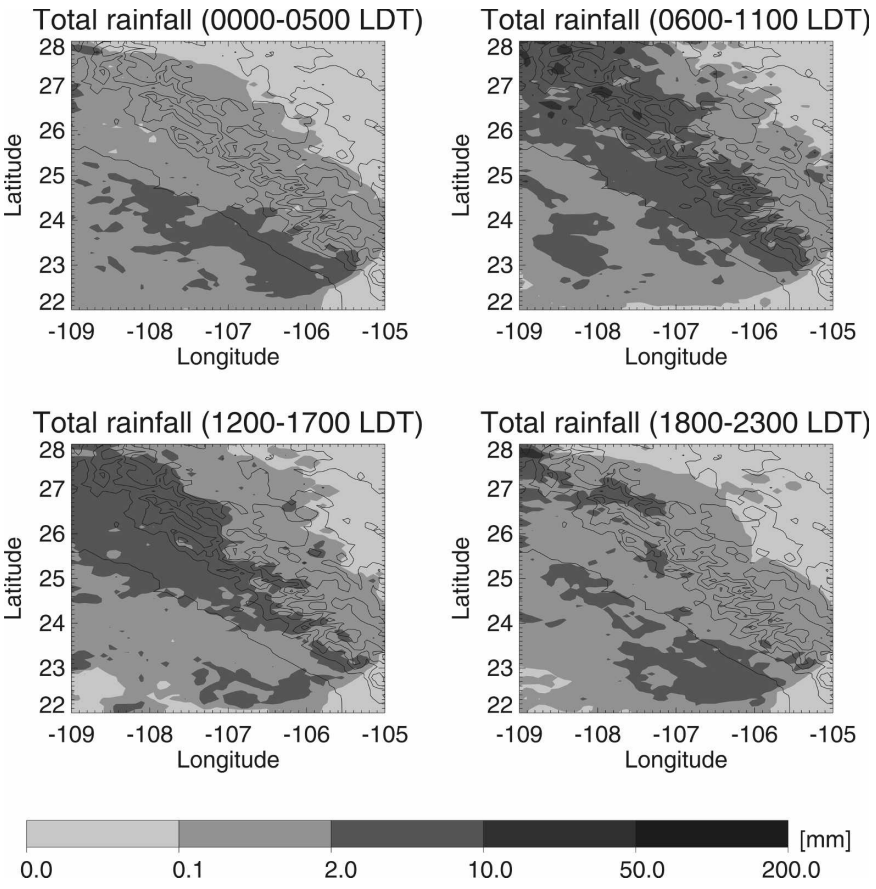

FIG. 4. Plots of smoothed total rainfall (mm), normalized by the number of points available at each grid point, for 6-h totals starting at 0000, 0600, 1200, and 1800 LDT, overlaid with smoothed topography. Topography is contoured from 0 to 3000 m in 500-m increments.

convective–stratiform partitioning to investigate features of both convective and stratiform precipitation in this region. Using S-Pol data, conditional averages of reflectivity as a function of height (MSL) and hour (LDT) were computed (Fig. 5). Only grid points with reflectivities greater than 0 dBZ are included [reflectivities were converted to linear units ($mm^6\ m^{-3}$) for averaging]. Also, the profiles do not extend above 12 km because there are so few points above this level such that the averages are heavily skewed toward the few higher reflectivities, yielding unrealistic profiles. Over the SMO (>2000 m), the most intense convection is confined to the afternoon hours consistent with the plots created from the 2D composites, but the greater reflectivities do not extend as high as the convection over the lower terrain. Reflectivities greater than 40 dBZ in the 0–1000 m elevation range occur, on average, during more times of the day than the other elevation groups, and extend to 5–6 km MSL during the late afternoon. Over water, these higher reflectivities are more limited to overnight and early morning hours, and are confined to lower heights compared to convection over land.

b. Land–water differences

A closer examination of differences between convection over land and water in the S-Pol domain is possible through comparisons of probability density functions (PDFs) for reflectivity (Figs. 6a,b). Differences between reflectivities over land and water are evident by an overall shift to greater frequencies over land for a given reflectivity band. This is especially noticeable for reflectivity bins greater than 30 dBZ, which show a greater occurrence of these reflectivity values at higher altitudes over land compared to over water, indicating that convective cells are more intense over land than over water. This tendency can also be seen in the diurnal plots presented in Fig. 3, especially in the afternoon when median rainfall rates over land are more than three times greater than over water. The exception is during the late morning when convection over land is a minimum prior to the initiation over the SMO. Johnson

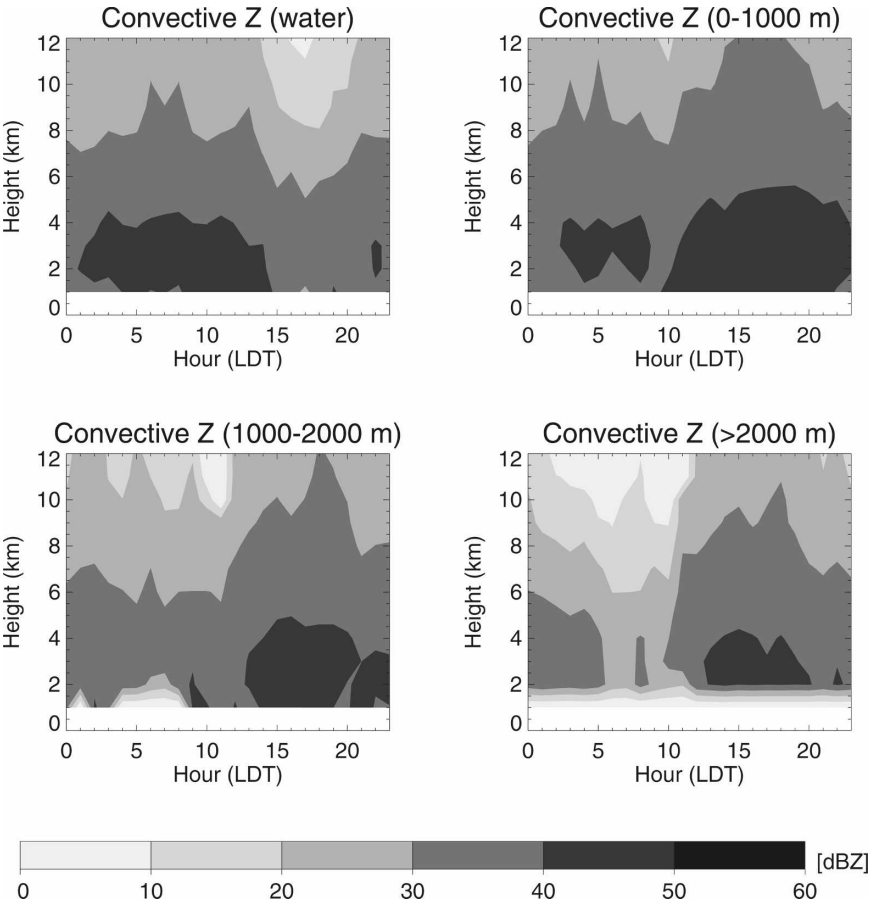

FIG. 5. Average reflectivities (dBZ) as a function of hour (LDT) and height (km) are displayed for each of the four elevation groups for convective precipitation. Averages are conditional in that they only include grid points with observed reflectivities greater than 0 dBZ.

et al. (2007) also observed this persistent diurnal cycle of strong convection over land and weak, infrequent convection over the Gulf of California. Using calculations of divergence, vertical motion, and heating, they found only weak upward motion associated with the less frequent convection over the water, principally in the lower troposphere. These results further suggest that during NAME, convection over land was more vertically intense with larger updrafts and occurrence of precipitation-sized ice above the 0°C level (at about 5 km) than convection over water.

c. Distributions of echo-top and 30-dBZ heights

To further investigate vertical characteristics of convection as a function of topography, echo-top heights using the S-Pol data are examined for each convective grid point with an observed rain rate greater than 0 mm h^{-1}. Although this grid column approach does not take into account the effects of shear on convection, significantly tilted updrafts appeared to be rare; therefore, it is a reasonable assumption that convective echo and rainfall at a particular grid point is associated with processes occurring directly over it in the same grid column (DeMott and Rutledge 1998). Echo-top heights are computed by determining the maximum height within the grid column at which reflectivity just exceeds 0 dBZ. Sensitivity tests were conducted for −5 and −10 dBZ but produced the same results as 0 dBZ. In addition to echo-top heights, the maximum height of the 30-dBZ contour is also computed to better understand the vertical intensity of convection during NAME. The choice of using the 30-dBZ contour is based on Zipser (1994) and Petersen et al. (1996) who found that lightning production, and therefore (inferred) larger supercooled water and ice water contents, is linked to the presence of the 30-dBZ contour above the freezing level.

Figures 7a,b show the number of convective points,

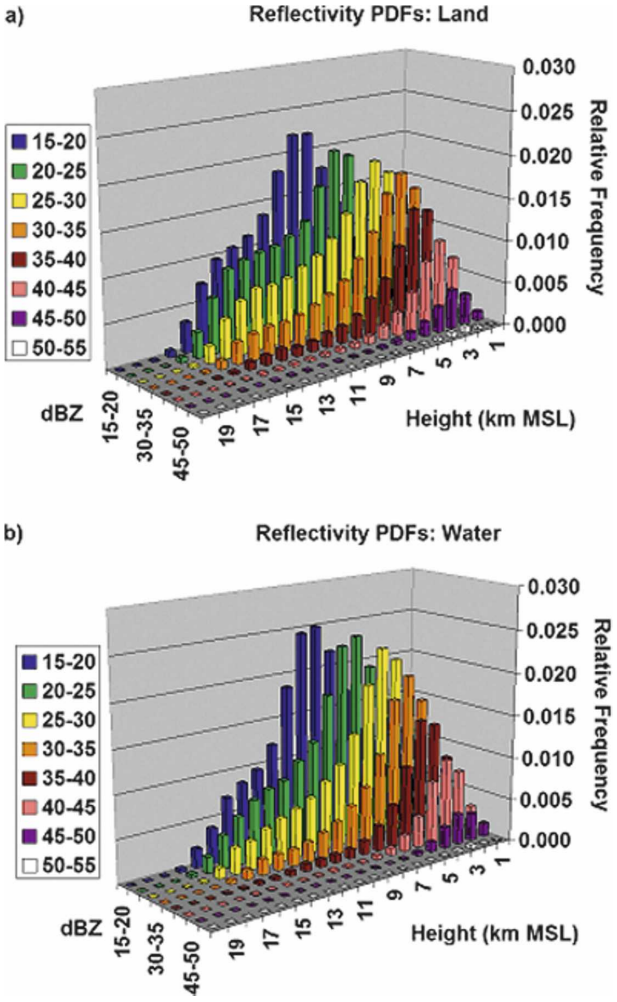

FIG. 6. Reflectivity PDFs as a function of height (km MSL) for (a) land and (b) water. Reflectivities are binned from 15 to 55 dBZ by 5-dBZ increments.

normalized by area, observed for a given echo-top height and maximum 30-dBZ contour heights for water and land, respectively. Similar to results from the 2D composites, convection in the S-Pol region, in general, occurs less frequently over water than land. However, an important feature that can be noted both over water and land are preferred peaks in echo-top heights near 5, 9, and 12 km, which can be roughly described as a trimodal distribution. A trimodal distribution in echo-top height occurrence was also observed in previous studies of tropical rainfall over the western Pacific Ocean. Johnson et al. (1999) described a structure in echo-top height characterized by three dominant levels that were in close proximity to prominent stable layers: 2 km (top of the trade stable layer), 5 km (near the melting level), and 15–16 km (tropopause). Convection impinging upon layers of higher stability can retard cloud growth and promote enhanced detrainment (Bretherton and Smolarkiewicz 1989).

To examine the effects of stability on convection in NAME, Fig. 8 shows the frequency distribution of temperature lapse rates exceeding certain thresholds for Mazatlan (located approximately 96 km from S-Pol, Fig. 1) using 156 soundings obtained during NAME. Although the relationship between levels of enhanced stability and peaks in echo-top height frequency is not as strong as observed in Johnson et al. (1999), there is a layer of increased stability between 5 and 6 km (near 0°C) suggesting that the prominent peak in echo-top heights near this level over land and water is associated with this layer of increased stability. This smaller layer of enhanced stability (slightly below 5 km) can be attributed to the effects of melting, whereas the larger peak about 1 km higher is likely due to radiative effects of the dry air layer (Mapes and Zuidema 1996) located directly over a moist layer (Fig. 9).

The peaks in frequency of echo-top height at 9 km and 12 km cannot be readily explained, since no obvious stable layers are evident at these levels (Fig. 8). To search for another possible explanation for the higher frequency of echo-top heights at 9 km, a contoured frequency by altitude diagram (CFAD) of relative humidity with respect to ice for Los Mochis is provided (Fig. 9). Although Los Mochis was located farther from S-Pol (297 km) compared to Mazatlan (Fig. 1), Los Mochis is chosen to represent the moisture content of the S-Pol environment because the Mazatlan soundings have a significant dry bias, especially at low levels (Johnson et al. 2007). Figure 9 shows that below 6 km, relative humidities (RH) generally range between 60% and 80%. Above this level, the range of observed RH increases dramatically, but with a greater frequency of very low RH and a mean of roughly 45%. Entrainment of this dry air into convection at these levels would be expected to reduce parcel buoyancy (Mapes and Zuidema 1996) and thus could provide an explanation for the observed peak in echo-top heights at 9 km. Analysis of equilibrium levels (EL) at soundings from Mazatlan and Los Mochis (not shown) indicate an average EL of about 13 km in this region. It is possible this level of reduced parcel buoyancy may provide an explanation for the observed peak in echo-top height around 12 km. Note also that no observations of echo-top height in Fig. 7 extend above 15 km because of the stabilizing influence of the tropopause, which was located around 15.5 km on average during NAME.

The normalized plots of echo-top and 30-dBZ height occurrences are also partitioned into the three elevation groups over land (Figs. 7c–e). The trimodal distribution of echo-top heights observed in the land plot

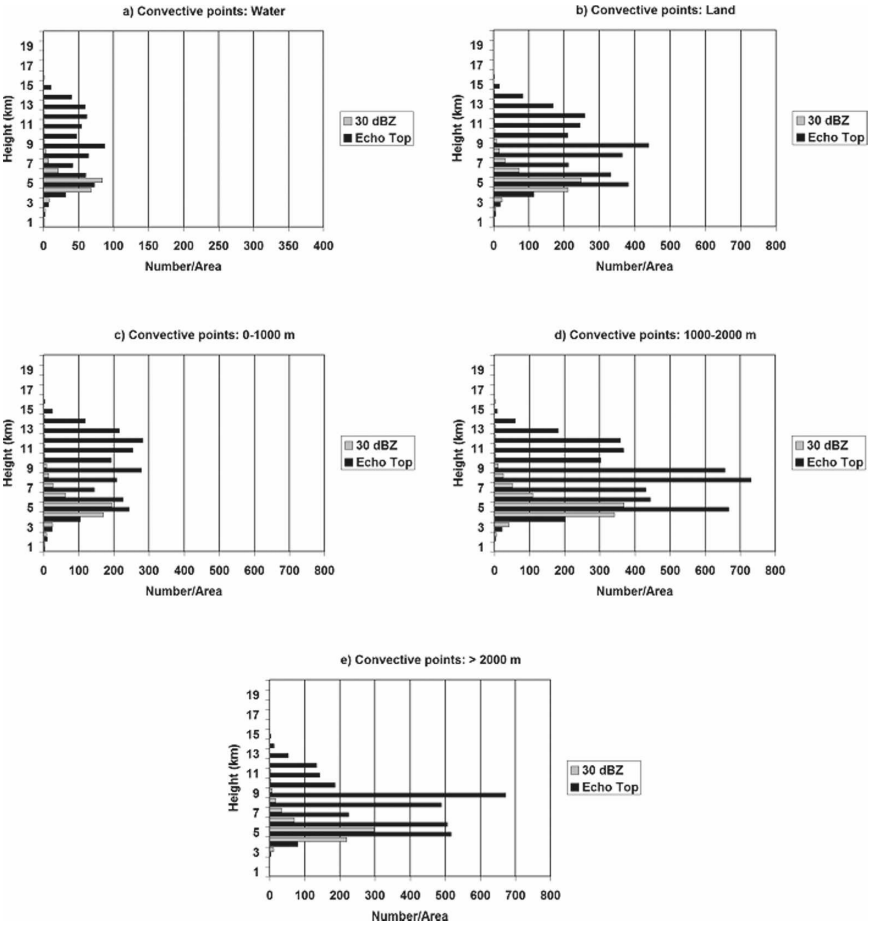

FIG. 7. Number of convective points observed from S-Pol with respect to echo-top heights and 30-dBZ heights for (a) over water, (b) all land, (c) 0–1000 m, (d) 1000–2000 m, and (e) >2000 m. Number of occurrence is normalized by the total area within the elevation group.

(Fig. 7a) is also present for the 0–1000-m and 1000–2000-m groups; however, only the peaks at 5 and 9 km are present over the SMO (>2000 m), suggesting that convection over the high terrain of the SMO is shallower than over the lower terrain. Nesbitt et al. (2008), using brightness temperatures from satellite observations, also found that convection over the higher terrain (>2250 m) is rarely of tropopause depth. They speculate that the observed maximum height of convection over the high terrain is limited by the lack of moisture available at cloud base relative to the lower elevations, thus significantly reducing the convective available potential energy (CAPE).

The diurnal variability of echo-top height distributions are examined in Fig. 10, which shows the occurrence of echo-top heights at 0000, 0600, 1200, and 1800 LDT. At local noon, the highest frequency of echo-top heights is concentrated over the higher terrain at about 5 km, reflecting the frequent shallow clouds initiating over the SMO. At 1800 LDT, higher echo-top heights are present over the SMO (10 km), but echo tops rarely extend to upper levels; at the same time, echo-top heights of greater than 12 km occur over the lower terrain. By midnight, there are overall fewer occurrences of all echo-top heights than during the evening, and by morning the majority of the deeper convection is concentrated over the lower terrain and adjacent waters with some shallower convection existing over the western slopes of the SMO. This diurnal variability in echo-top height distributions suggests that the observed higher-intensity precipitation over the lower terrain at night is associated with deeper convection compared to the shallower convection over the SMO that produces more frequent, but less intense rainfall.

Although there is a noticeable difference in echo-top height distributions with respect to terrain (Figs. 7a–e), 30-dBZ heights are similar for each elevation group with normal-like distributions peaking around 5 km

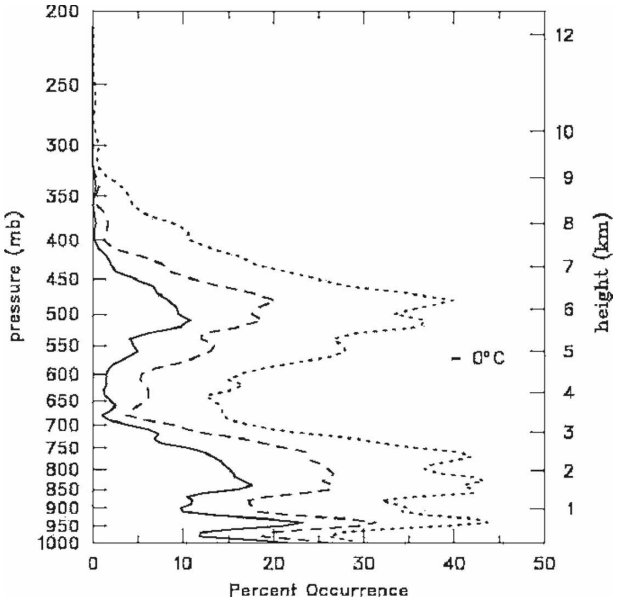

FIG. 8. Cumulative frequency (%) of stability (dT/dz) greater than $-5°$ (solid), $-4°$ (dashed), and $-3°C\ km^{-1}$ (dotted) for Mazatlan (23.2°N, 106.4°W) using 156 soundings during NAME.

(Figs. 7a,e). DeMott and Rutledge (1998) found similar results when comparing radar data obtained from multiple cruises aboard research vessel (R/V) *Vickers* during the Tropical Ocean and Global Atmosphere Coupled Ocean–Atmosphere Response Experiment (TOGA COARE). They concluded that despite the differences in echo-top height between cruises, convection, whether shallow or deep, was just as intense in terms of rainfall as shown by the observed similarities

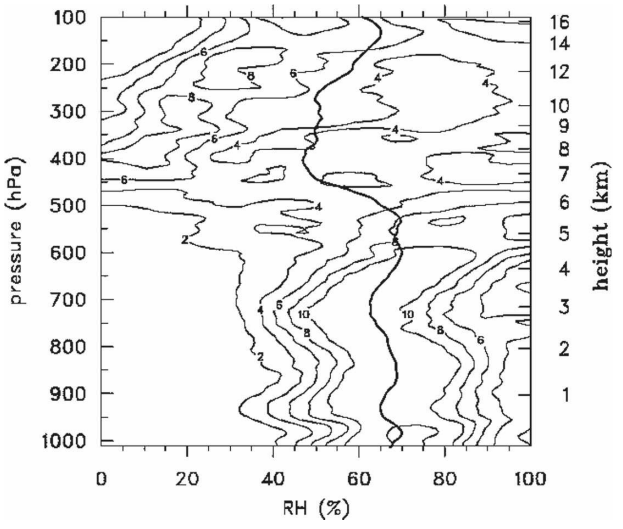

FIG. 9. CFAD of relative humidity with respect to ice for Los Mochis (25.7°N, 109.1°W). The solid line represents the mean relative humidity profile for the 207 soundings.

in 30-dBZ distributions. For NAME, however, surface rainfall rates differ with elevation. Therefore, the 30-dBZ contour is not an accurate representation of the intensity of the precipitation, suggesting there are other factors, such as cloud depth below this level, that need to be considered (discussed in section 5 below).

d. Comparison of NAME convection with other tropical locales

In addition to analyses of echo-top and 30-dBZ heights, the contribution to convective rainfall as a function of echo-top height from NAME is compared with all events during TOGA COARE, a study focusing on characteristics of tropical convection over ocean (Webster and Lukas 1992). In Fig. 11, the TOGA COARE information, adapted from Johnson et al. (1999), reveals a similar structure to that for convection over water and land in NAME, in which all three distributions exhibit a secondary peak at 9 km and a primary peak at a higher echo-top height. Convection over land during NAME peaks again at 12 km; however, the convection over water in NAME and the TOGA COARE convective cells peak at 14 km. The faster drop-off in height of the NAME convective rainfall profiles is likely associated with a lower tropopause in the NAME region (about 15.5 km versus about 17 km in TOGA COARE). In general, both tropical locales observed a similar trend of greater contributions of tropical convective rainfall tending to be produced by convection with taller echo-top heights.

Vertical trends in reflectivity during NAME are compared to reflectivity PDFs (similar to Figs. 6a,b) constructed from radar data from the Tropical Rainfall Measuring Mission/Large-Scale Biosphere–Atmosphere Experiment in Amazonia (TRMM/LBA; Fig. 12a) and the Eastern Pacific Investigation of Climate Processes in the Coupled Ocean–Atmosphere System (EPIC; Fig. 12b), obtained from Pereira and Rutledge (2006). Details regarding the easterly/westerly (TRMM/LBA) and northerly/southerly phases (EPIC) can also be found in Pereira and Rutledge (2006). The distribution of reflectivity for TRMM/LBA, which was conducted over land, is similar to the overland portion of the NAME convection, with more frequent observations of 30–35-dBZ heights at greater heights. This is in comparison to NAME convection over water and EPIC (an overwater experiment; Raymond et al. 2004); both are characterized by a greater occurrence of higher reflectivities at lower levels than the convection over land. Frequent observations of reflectivities over 45 dBZ do occur at greater heights for the easterly regime of TRMM/LBA (relative to westerly; Fig. 12a) and northerly regime of EPIC (relative

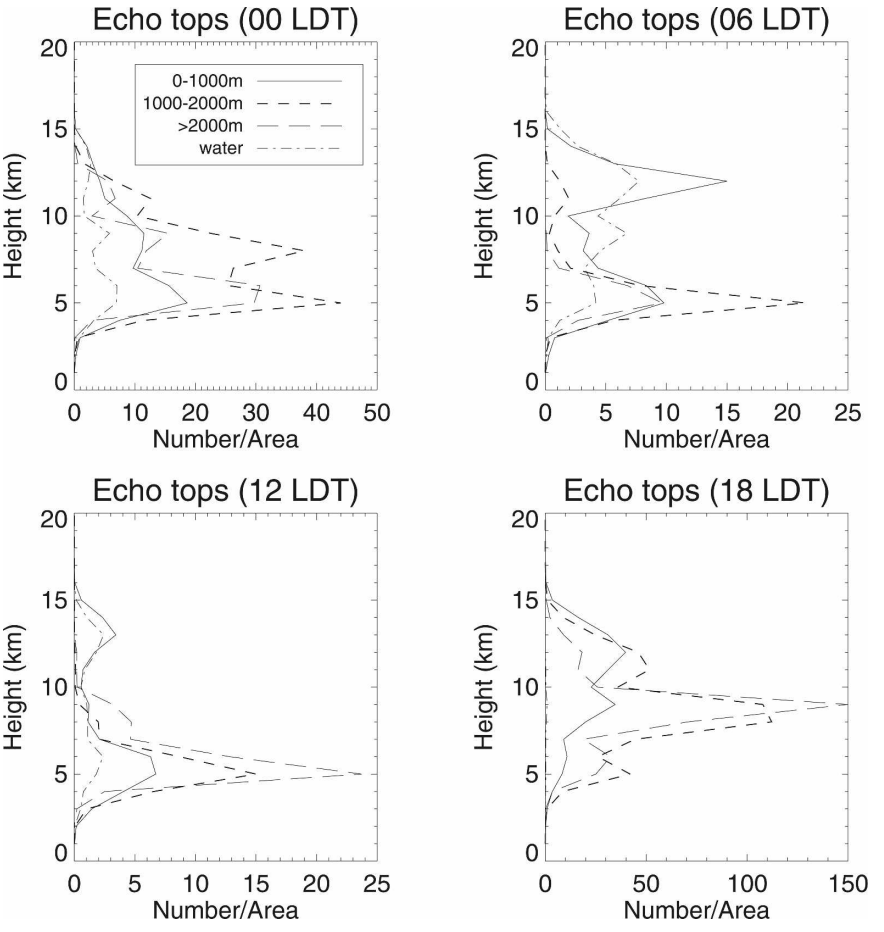

FIG. 10. Number of convective points observed from S-Pol with respect to echo-top heights and time of day (LDT). Number of occurrence is normalized by the total area within the elevation group. Note the *x* axes are not on the same scale.

to southerly; Fig. 12b); however, the occurrence of these higher reflectivities extend to even higher heights during NAME (roughly 7 km MSL) for both land and water (Figs. 6a,b). This indicates that the precipitating systems during NAME, in general, were often deeper than those observed during EPIC and TRMM/LBA.

5. Analysis of warm-cloud depths as a function of topography

Although it has been shown that echo-top heights over the lower terrain in NAME are higher than over the SMO, this does not necessarily explain the observed trend in rainfall intensity with respect to terrain (larger peak rain rates over low terrain compared to over the highest terrain). We now investigate possible differences in warm-cloud depths with elevation, and the role these differences may contribute to peak rainfall intensity as a function of elevation. Deeper warm-cloud depths provide for more coalescence growth as melting ice particles fall through this layer and accrete available liquid water. Nesbitt et al. (2008) demonstrated the tendency for convection over the western slopes of the SMO to be comparatively shallow, with cloud-base heights, estimated using a method from Stull (1995), of less than 1.0 km (AGL) on average. For this study, lifting condensation levels (LCLs) and melting levels are computed to further investigate this variation in depth with elevation.

The NAME radiosonde dataset, profiler wind data from the NCAR Integrated Sounding System (ISS) sites, Quick Scatterometer (QuikSCAT) retrieved surface oceanic winds, and aviation routine weather report (METAR) surface reports are used to objectively analyze surface and upper-air fields at 6 h, 1° horizontal and 25-hPa vertical resolution over the domain from 22°–35°N, 115°–100°W, referred to as the T1A domain (Johnson et al. 2007). Analyzed fields used in this study

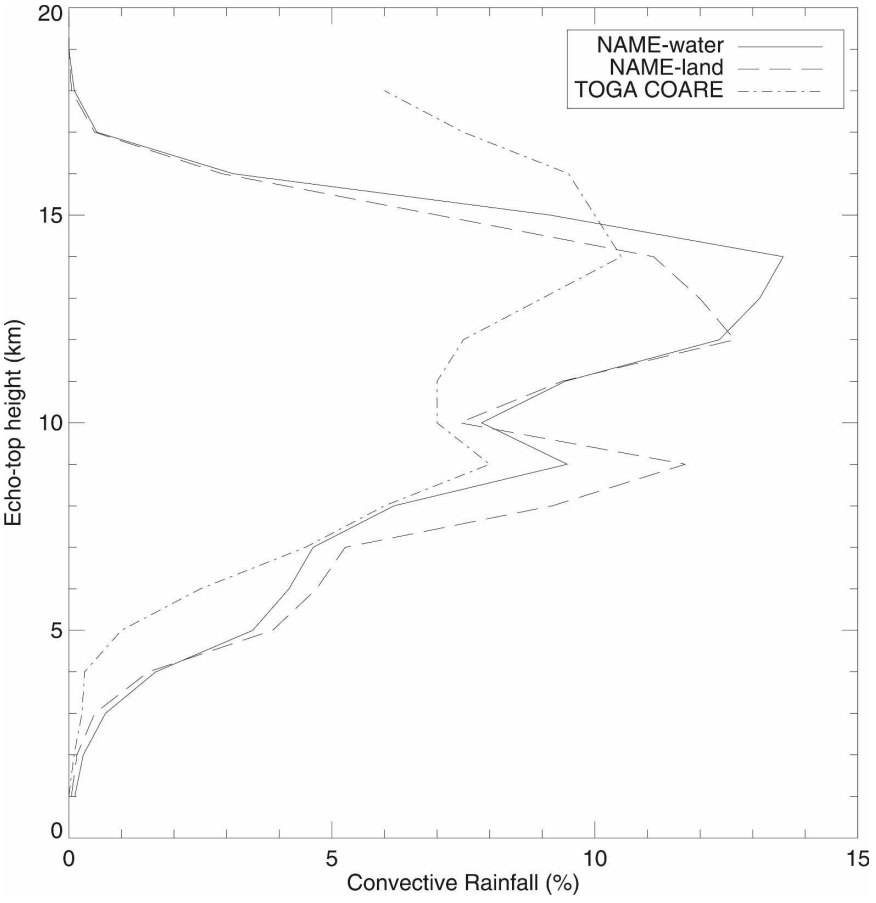

FIG. 11. Comparison of contribution to convective rainfall from NAME (land and water) and TOGA COARE (all water). Information for TOGA COARE is adapted from Johnson et al. (1999) for all events.

include geopotential height (m), temperature (°C), water vapor mixing ratio (g kg^{-1}), and surface pressure (mb) from the version 3 Colorado State University (CSU) gridded analyses (Johnson et al. 2007). Data are available at 0000, 0600, 1200, and 1800 UTC for 7 July through 15 August and are used to compute LCLs and melting levels over each of the 1° grid points.[1] The LCL is computed by decreasing the temperature of the surface parcel dry adiabatically with height, using this temperature to compute the saturation mixing ratio at each vertical level, then determining the minimum level at which the computed saturation mixing ratio is equal to the observed surface water vapor mixing ratio. In some cases, especially over the higher terrain, this condition is not met above ground level; therefore, over the SMO, LCLs are given the value of the local terrain elevation. Observations during NAME indicate that cloud bases frequently intercept the higher terrain of the SMO, making this a reasonable assumption (Nesbitt et al. 2008). Figure 13 displays a cross section at 24°N (shown in Fig. 1) of the LCLs (MSL) averaged over the EOP during NAME for the region between 109° and 105°W. The average LCL increases in height with increasing elevation, and provides a rough estimate of a cloud-base height of about 0.5 km MSL over the lower terrain, which increases to approximately 2.5 km MSL over the SMO; these estimates are consistent with cloud-base heights computed by Nesbitt et al. (2008).

The melting level is estimated by finding the minimum level at which the observed temperature falls between −4° and −1.5°C; these values are chosen to avoid brightband contamination when computing statistics at this level. The average melting level for the T1

[1] Upper-air gridded analyses over the SMO represent an interpolation from sounding sites on the western Mexican coast to sites a few hundred kilometers to the east of the SMO crest and thus may not accurately represent conditions over higher elevations. Therefore, caution should be taken when using these results for analyses other than qualitative comparisons.

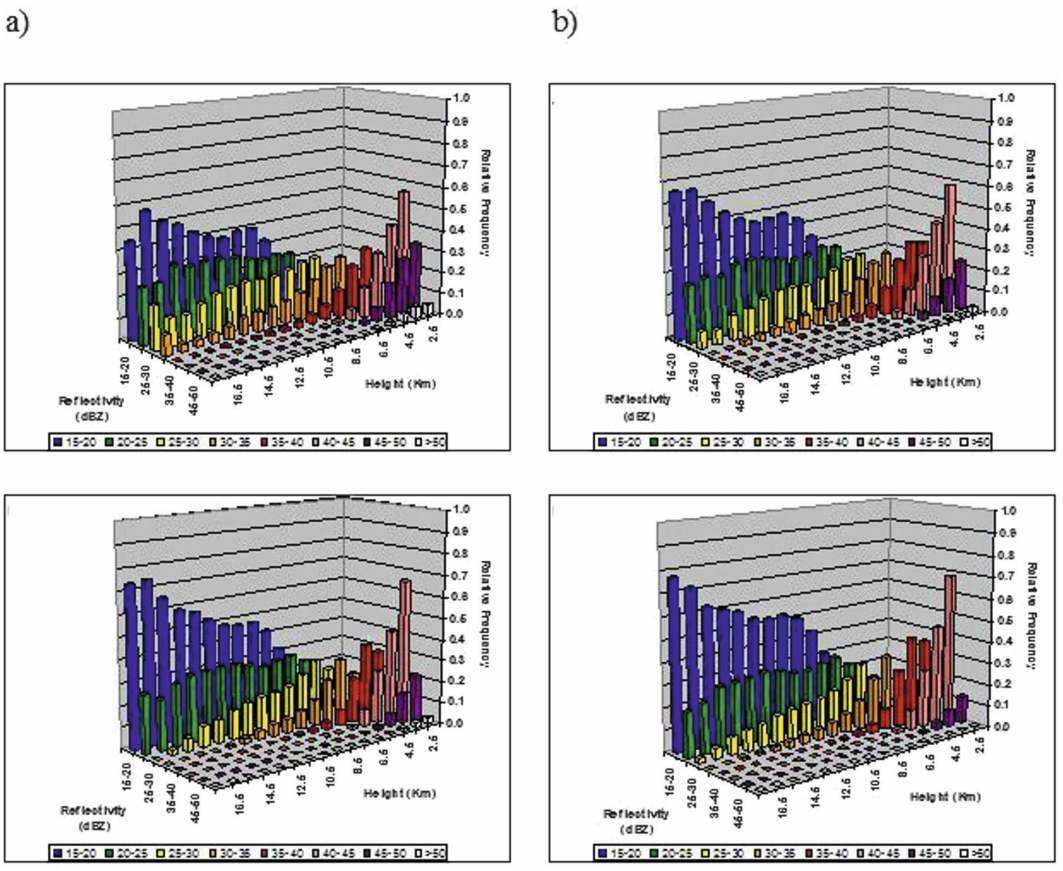

FIG. 12. Reflectivity PDFs adapted from Pereira and Rutledge (2006) for (a) TRMM/LBA and (b) EPIC. The top (bottom) panels represent the easterly (westerly) and northerly (southerly) regimes for TRMM/LBA and EPIC, respectively.

domain is approximately 5 km (dashed line in Fig. 13), consistent with radar observations, and coinciding with the layer of enhanced stability at roughly 5 km observed from the Mazatlan sounding. Average warm-cloud depths, computed by finding the difference between the LCL and melting level, are shown in Fig. 13. The depth of the warm-rain coalescence zone is found to decrease with increasing elevation, as expected, reflecting the shallower convection over the SMO compared to over the coast. Average warm-cloud depths vary from roughly 4500 m over the lower terrain to 2500 m over the highest elevations of the SMO.

It is hypothesized that the variations in warm-cloud depth between the higher and lower terrain are the major contributor to the observed differences in precipitation intensity with elevation. To test this hypothesis, a simplified model of stochastic drop growth from the Colorado State University Regional Atmospheric Modeling System (RAMS) microphysics algorithm (Saleeby and Cotton 2004) is used to simulate average rain rates with varying warm-cloud depths. A homogenous cloud layer of 5 km is initially assumed above the melting level; additional details regarding the model simulation and assumptions are described in the appendix. Average precipitation rates for warm-cloud depths of 2500, 3500, and 4500 m are determined after a 30-min model run, at which point the final rain spectrum achieves equilibrium. These results are then normalized by the maximum simulated rain rate to determine the relative effect of warm-cloud depth on rainfall intensity. Normalized rain rates decrease from 1.00 to 0.86 to 0.73 for warm-cloud depths of 4500, 3500, and 2500 m, respectively, indicating that decreasing warm-cloud depth leads to a decrease in average rainfall rate. For comparison, average convective rainfall rates are computed from the entire 2D radar composite domain and normalized by the highest observed average to obtain a value of 1.00 over the coastal plain (0–1000 m) where warm-cloud depths are roughly 4500 m. For elevations in the 1000–2000-m range, where warm-cloud depths are on the average 3500 m, the relative rain rate reduced to 0.94, and over the SMO (warm-cloud depth

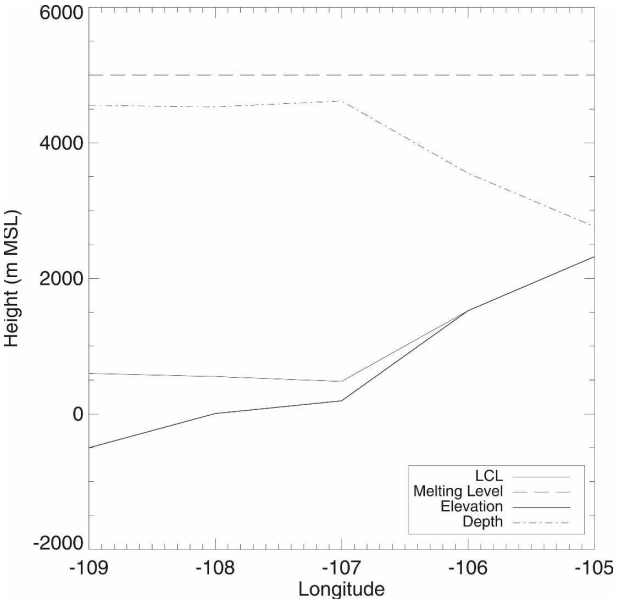

FIG. 13. The average LCLs, melting level, smoothed elevations, and warm-cloud depths are plotted for a cross section along 24°N (line shown in Fig. 1). Average warm-cloud depths are determined as the difference in height between the melting level and the LCL. Elevation values less than 0 m indicate water.

approximately 2500 m), the observed rainfall rate is only 0.61 of that observed over the coast. Although the magnitude of the reduction between simulated and observed rates is slightly different, the simulated trend of decreasing convective precipitation intensity with decreasing warm-cloud depth, and therefore increasing elevation, agrees with the observed trend. This similar trend suggests that the differences in warm-cloud depth across elevation groups may explain differences in peak rain rates with respect to elevation.

The previously described model simulation assumed a cloud layer of 5 km above the melting level for all warm-cloud depths; however, recall from Fig. 7 that echo-tops are generally higher over the lower terrain than over the peaks of the SMO. To account for the shallower convection over the SMO, average rain rates are produced from the model for a homogenous cloud layer of 1 km above the melting level, with all other assumptions remaining the same. Average precipitation intensities were reduced more for decreasing warm-cloud depths than for the 5-km layer. Specifically, decreasing the warm-cloud depth from 4500 to 2500 m for this revised simulation reduced the average precipitation by 61%, compared to the 73% reduction for the 5-km layer. The magnitude of this reduction is the same as the observed decrease in rain rate over the SMO, where warm-cloud depths are approximately 2500 m and echo-top heights are generally lower than over the coast. This suggests that warm-rain processes are the dominant factor for precipitation over the highest terrain; however, in addition to warm-rain depth, the processes that occur above the melting level need to be considered to fully explain the observed trend in rainfall intensity over the lower terrain. The polarimetric information available from S-Pol will be valuable for investigating differences in the microphysics of the precipitating systems to improve understanding of the processes occurring in the core monsoon region.

6. Summary and conclusions

The North American Monsoon Experiment radar network provided unprecedented observations of precipitation systems within the North American monsoon. Diurnal characteristics of precipitation are poorly represented in numerical simulations of the NAM (e.g., Collier and Zhang 2007); therefore, this study aims to contribute to the basic understanding of trends in precipitation intensity and frequency as a function of time of day as well as local terrain. Cumulative distribution functions of rainfall totals, computed from the 2D rain-rate composites from the radar network, reveal a transition to heavier precipitating events with decreasing elevation. The greater separation between elevation groups for the daily rain totals compared to the 15-min totals suggests the possibility for intense precipitation to occur over the foothills of the SMO, but these events are not as likely to be sustained for the same duration as those over the lower terrain. These results are consistent with trends found using the NAME Event Rain Gauge Network from Gochis et al. (2007); therefore validating these results using an independent dataset. A pronounced diurnal trend in precipitation frequency and intensity is observed using the 2D rain-rate composites from the NAME radar network. Also consistent with NERN results, the diurnal cycle is characterized by frequent precipitation initiating over the SMO around 1600 LDT (UTC − 6). This precipitation organizes as it propagates toward the coast in the time-mean easterly flow, leading to high intensity, but less frequent precipitation over the lower terrain during the late night–early morning hours.

Elevation-dependent trends in precipitating features were further investigated using a 3D dataset created from S-Pol. Each of these grid points was subjected to a convective–stratiform partitioning algorithm based on Yuter and Houze (1997, 1998), and vertical profiles of reflectivity were constructed for both convective and stratiform precipitation. These profiles indicate a tendency for precipitation, especially convective, to be

more vertically intense over the lower terrain than over the SMO. Analysis of the diurnal cycle of these reflectivity profiles show that the most intense convection over the low terrain, in terms of reflectivity, occurs during the evening and early morning. The intense convection that occurs over the SMO is limited to the afternoon, consistent with diurnal trends of near-surface precipitation observed using the 2D composites from the entire network. Reflectivity information provided by the S-Pol composites also allowed for analysis of echo-top height distributions as a function of terrain. Over both land and water, there is a tendency for a trimodal distribution in echo-top heights, with peaks at 5, 9, and 12 km. The peaks at 5 and 12 km may be explained by layers of enhanced stability present near these levels (melting level and equilibrium level, respectively) that limit vertical growth of convection, whereas the peak observed at 9 km is likely due to dry air entrainment. The peak at 12 km is absent over the SMO, indicating the tendency for convection over the higher terrain to be shallower than over the coast.

To investigate possible explanations for the observed trends in precipitation frequency and intensity, the CSU–NAME upper-air and surface gridded analyses were used to compute average LCLs and melting levels to compare warm-cloud depths over the various elevation groups. As hypothesized, there is a decreasing trend in warm-cloud depth with increasing elevation, with values ranging from an average of 4500 m over the lowest terrain to 2500 m over the SMO. A simplified model of stochastic droplet growth from the Colorado State University RAMS microphysics algorithm was used to determine the impact of these differences in warm-cloud depth on precipitation intensity. The model allowed an assumed initial drop size distribution to fall through the melting level and grow through coalescence for 30 min to determine average precipitation rates. The simulated trend of decreasing convective precipitation intensity with decreasing warm-cloud depth (increasing elevation) corresponds to the observed trend, suggesting that the differences in warm-cloud depth between elevation groups could explain the differences in rainfall rates with respect to elevation.

There is a vast amount of polarimetric data collected from S-Pol during NAME that may provide further details regarding the microphysical variability of convection as a function of terrain. This study only analyzed warm-rain processes; however, the polarimetric information will allow for analysis of ice processes to provide a better understanding of trends in rainfall production. These detailed analyses could aid in further understanding of the elevation-dependent diurnal characteristics of convection in the core monsoon region, and ultimately improve prediction of warm-season precipitation associated with the North American monsoon. The variability of mesoscale organization and the interaction of gust fronts with the sea breeze over the coastal plain in contributing to rainfall variability will also be the subject of future studies.

Acknowledgments. We thank the S-Pol radar staff from the Earth Observing Laboratory (EOL) of NCAR—in particular the lead S-Pol engineers, Don Ferraro and Jon Lutz, and science staff, Tammy Weckwerth, James Wilson, and Jothiram Vivekanandan. Rit Carbone of NCAR (Co-PI on the S-Pol deployment) was critical to making radar observations in NAME a success. John Lutz, along with the assistance of Arturo Valdez-Manzanilla of Juarez University and Armando Rodriguez Davila of SMN, led the SMN radar upgrade and data collection efforts. Initial quality control and distribution of radar data was led by Bob Rilling of NCAR EOL, and further quality control of the data was aided by Chad Christenson, Lee Nelson, and Gustavo Pereira of Colorado State University. We thank Gustavo Pereira also for his assistance in optimizing the convective–stratiform partitioning algorithm. We also thank Dr. Rob Cifelli, Dr. Stephen Nesbitt, and Paul Hein for insightful discussion and assistance in computer programming issues. Radar observations and analyses were funded by the National Oceanic and Atmospheric Administration (SMN radars) Grant NA17RJ1228 and the National Science Foundation (S-Pol) Grant ATM-0340544. Paul Ciesielski was supported by NASA Grant NNG04GA22G.

APPENDIX

Details and Simplifications of the RAMS Stochastic Growth Scheme

RAMS uses a bin-emulating approach to explicitly simulate the warm-rain, collision–coalescence process by the method of moments (Tzivion et al. 1987). In this scheme, an initial exponential droplet size distribution of hydrometeors is decomposed into 36 mass-doubling bins for two moments of the distribution (mixing ratio and number concentration; Saleeby and Cotton 2004). Bin collection interactions are then computed using realistic collection efficiencies and the hydrometeor distributions are reconstructed from the updated bins. Evolution of the hydrometeor spectra is predicted through vapor deposition/evaporation, stochastic coalescence, and sedimentation (Walko et al. 1995; Meyers et al. 1997). For this study, evaporation was ignored, which did not alter the results significantly, and the

initial distribution of hydrometeors was only allowed to grow through collection of cloud droplets in the warm-cloud layer.

Further simplifications to the RAMS stochastic growth scheme include assuming an initial rain mixing ratio of 2 g kg^{-1} and an initial drop concentration of 3800 m^{-3}, yielding an initial average drop diameter of 1 mm. These parameters are specified at the 5-km MSL level, corresponding to the 0°C level and, therefore, the top of the warm-cloud zone. This drop size diameter results in an initial reflectivity of about 36 dBZ, corresponding to a rain rate of approximately 10 mm h^{-1}, which is similar to the observed initial average precipitation rate of 17 mm h^{-1}. This observed precipitation rate was computed by determining the average reflectivity at 5 km, then applying the Z–R relationship used in the composites to determine an estimated rainfall rate at this level. The distribution of hydrometeors with these characteristics then falls through the warm-cloud region, containing an initial cloud droplet concentration of 300 cm^{-3}. A typical value for cloud liquid water of 1 g kg^{-1} is used, giving an initial average cloud droplet diameter of 18 μm. A cloud droplet concentration of 100 cm^{-3} was also tested, but changes in the results were minimal. This increase in diameter results in a higher collection efficiency, but is counteracted by the decreased amount of droplets to collect, therefore balancing each other and resulting in almost no change in precipitation rates. Autoconversion is turned off to only allow for collection of cloud droplets by raindrops (i.e., no self-collection of cloud droplets allowed).

REFERENCES

Adams, D. K., and A. C. Comrie, 1997: The North American monsoon. *Bull. Amer. Meteor. Soc.,* **78,** 2197–2213.

Bretherton, C. S., and P. K. Smolarkiewicz, 1989: Gravity waves, compensating subsidence and detrainment around cumulus clouds. *J. Atmos. Sci.,* **46,** 740–759.

Bringi, V. N., T. Tang, and V. Chandrasekar, 2004: Evaluation of a new polarimetrically based Z–R relation. *J. Atmos. Oceanic Technol.,* **21,** 612–623.

Cifelli, R., W. A. Petersen, L. D. Carey, S. A. Rutledge, and M. A. F. da Silva Dias, 2002: Radar observations of the kinematic, microphysical, and precipitation characteristics of two MCSs in TRMM LBA. *J. Geophys. Res.,* **107,** 8077, doi:10.1029/2000JD000264.

Collier, J. C., and G. J. Zhang, 2007: Effects of increased horizontal resolution on simulations of the North American monsoon in the NCAR CAM3: An evaluation based on surface, satellite, and reanalysis data. *J. Climate,* **20,** 1843–1861.

DeMott, C. A., and S. A. Rutledge, 1998: The vertical structure of TOGA COARE convection. Part I: Radar echo distributions. *J. Atmos. Sci.,* **55,** 2730–2747.

Douglas, M., R. A. Maddox, K. Howard, and S. Reyes, 1993: The Mexican monsoon. *J. Climate,* **6,** 1665–1677.

Doviak, R. J., and D. S. Zrnic, 1993: *Doppler Radar and Weather Observations*. Academic Press, 562 pp.

Farfán, L. M., and J. A. Zehnder, 1994: Moving and stationary mesoscale convective systems over northwest Mexico during the Southwest Area Monsoon Project. *Wea. Forecasting,* **9,** 630–639.

Gochis, D. J., J. C. Leal, C. J. Watts, W. J. Shuttleworth, and J. Garatuza-Payan, 2003: Preliminary diagnostics from a new event-based monitoring system network in support of the North American Monsoon Experiment (NAME). *J. Hydrometeor.,* **4,** 974–981.

——, A. Jimenez, C. J. Watts, J. Garatuza-Payan, and W. J. Shuttleworth, 2004: Analysis of 2002 and 2003 warm-season precipitation from the North American Monsoon Experiment event rain gauge network. *Mon. Wea. Rev.,* **132,** 2938–2953.

——, L. Brito-Castillo, and W. J. Shuttleworth, 2006: Hydroclimatology of the North American monsoon region in northwest Mexico. *J. Hydrol.,* **316,** 53–70.

——, C. J. Watts, J. Garatuza-Payan, and J. Cesar-Rodriguez, 2007: Spatial and temporal patterns of precipitation intensity as observed by the NAME event rain gauge network from 2002 to 2004. *J. Climate,* **20,** 1734–1750.

Higgins, R. W., Y. Yao, and X. Wang, 1997: Influence of the North American monsoon system on the U.S. summer precipitation regime. *J. Climate,* **10,** 2600–2622.

——, and Coauthors, 2006: The NAME 2004 field campaign and modeling strategy. *Bull. Amer. Meteor. Soc.,* **87,** 79–94.

Janowiak, J. E., V. E. Kousky, and R. J. Joyce, 2005: Diurnal cycle of precipitation determined from the CMORPH high spatial and temporal resolution global precipitation analyses. *J. Geophys. Res.,* **110,** D23105, doi:10.1029/2005JD006156.

Johnson, R. H., T. M. Rickenbach, S. A. Rutledge, P. E. Ciesielski, and W. H. Schubert, 1999: Trimodal characteristics of tropical convection. *J. Climate,* **12,** 2397–2418.

——, P. E. Ciesielski, B. D. McNoldy, P. J. Rogers, and R. K. Taft, 2007: Multiscale variability of the flow during the North American Monsoon Experiment. *J. Climate,* **20,** 1628–1648.

Lang, T. J., D. A. Ahijevych, S. W. Nesbitt, R. E. Carbone, S. A. Rutledge, and R. Cifelli, 2007: Radar-observed characteristics of precipitating systems during NAME 2004. *J. Climate,* **20,** 1713–1733.

Mapes, B. E., and P. Zuidema, 1996: Radiative-dynamical consequences of dry tongues in the tropical atmosphere. *J. Atmos. Sci.,* **53,** 620–638.

Meyers, M. P., R. L. Walko, J. Y. Harrington, and W. R. Cotton, 1997: New RAMS cloud microphysics parameterization. Part II. The two-moment scheme. *Atmos. Res.,* **45,** 3–39.

Mock, C. J., 1996: Climatic controls and spatial variations of precipitation in the western United States. *J. Climate,* **9,** 1111–1125.

Negri, A. J., R. F. Adler, E. J. Nelkin, and G. J. Huffman, 1994: Regional rainfall climatologies derived from Special Sensor Microwave Imager (SSM/I) data. *Bull. Amer. Meteor. Soc.,* **75,** 1165–1182.

Nesbitt, S. W., D. J. Gochis, and T. J. Lang, 2008: The diurnal cycle of clouds and precipitation along the Sierra Madre Occidental observed during NAME-2004: Implications for warm season precipitation estimation in complex terrain. *J. Hydrometeor.,* **9,** 728–743.

Pereira, L. G., and S. A. Rutledge, 2006: Diurnal cycle of shallow and deep convection for a tropical land and an ocean envi-

ronment and its relationship to synoptic wind regimes. *Mon. Wea. Rev.,* **134,** 2688–2701.

Petersen, W. A., S. A. Rutledge, and R. E. Orville, 1996: Cloud-to-ground lightning observations from TOGA COARE: Selected results and lightning location algorithms. *Mon. Wea. Rev.,* **124,** 602–620.

Raymond, D. J., and Coauthors, 2004: EPIC2001 and the coupled ocean–atmosphere system of the tropical east Pacific. *Bull. Amer. Meteor. Soc.,* **85,** 1341–1354.

Rickenbach, T. M., and S. A. Rutledge, 1998: Convection in TOGA COARE: Horizontal scale, morphology, and rainfall production. *J. Atmos. Sci.,* **55,** 2715–2729.

Saleeby, S. M., and W. R. Cotton, 2004: A large droplet mode and prognostic number concentration of cloud droplets in the Colorado State University Regional Atmospheric Modeling System (RAMS). Part I: Module descriptions and supercell test simulations. *J. Appl. Meteor.,* **43,** 182–195.

Steiner, M., R. A. Houze Jr., and S. E. Yuter, 1995: Climatological characteristics of three-dimensional storm structure from operational radar and rain gauge data. *J. Appl. Meteor.,* **34,** 1978–2007.

Stull, R. B., 1995: *Meteorology Today for Scientists and Engineers*. West Publishing, 385 pp.

Tzivion, S., G. Feingold, and Z. Levin, 1987: An efficient numerical solution to the stochastic collection equation. *J. Atmos. Sci.,* **44,** 3139–3149.

Walko, R. L., W. R. Cotton, M. P. Meyers, and J. Y. Harrington, 1995: New RAMS cloud microphysics parameterization: Part I: The single-moment scheme. *Atmos. Res.,* **38,** 29–62.

Webster, P. J., and R. Lukas, 1992: TOGA COARE: The Coupled Ocean–Atmosphere Experiment. *Bull. Amer. Meteor. Soc.,* **73,** 1377–1416.

Yuter, S. E., and R. A. Houze Jr., 1997: Measurements of raindrop size distributions over the Pacific warm pool and implications for *Z–R* relations. *J. Appl. Meteor.,* **36,** 847–867.

——, and ——, 1998: The natural variability of precipitating clouds over the western Pacific warm pool. *Quart. J. Roy. Meteor. Soc.,* **124,** 53–99.

Zipser, E. J., 1994: Deep cumulonimbus cloud systems in the tropics with and without lightning. *Mon. Wea. Rev.,* **122,** 1837–1851.